Journal Pre-proof

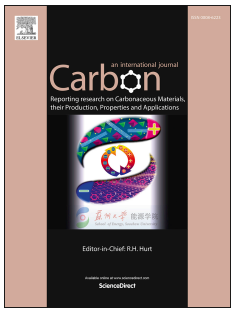

Rapid Joule-heating-driven synthesis of FeCo alloy nanoparticles embedded in porous carbon nanorods for electromagnetic wave absorption

Letian Huang, Chunhui Bai, Jinyu Jia, Yujin Chen, Chunling Zhu, Xinzhi Ma, Xiao Zhang

PII: S0008-6223(25)00608-6

DOI: https://doi.org/10.1016/j.carbon.2025.120592

Reference: CARBON 120592

To appear in: *Carbon*

Received Date: 9 June 2025

Revised Date: 29 June 2025

Accepted Date: 2 July 2025

Please cite this article as: L. Huang, C. Bai, J. Jia, Y. Chen, C. Zhu, X. Ma, X. Zhang, Rapid Joule-heating-driven synthesis of FeCo alloy nanoparticles embedded in porous carbon nanorods for electromagnetic wave absorption, *Carbon*, https://doi.org/10.1016/j.carbon.2025.120592.

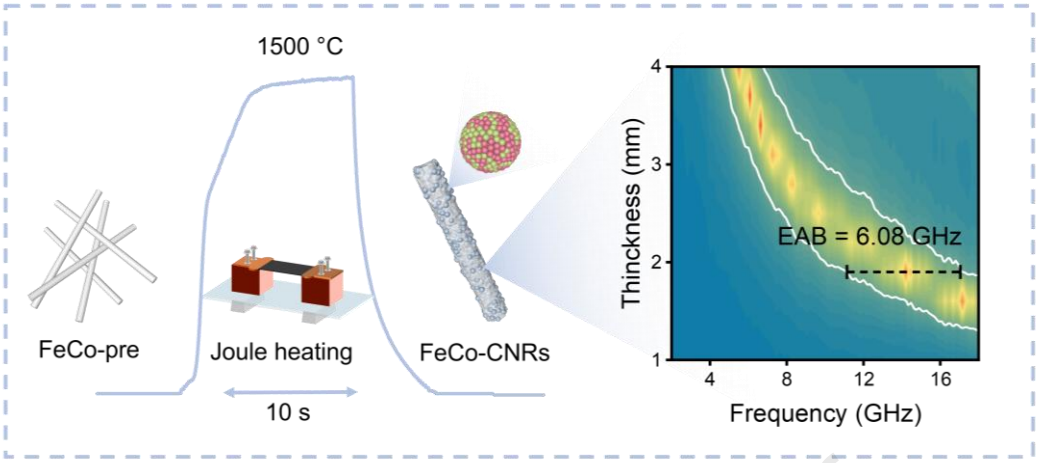

Rapid Joule-heating-driven synthesis of FeCo alloy nanoparticles embedded in porous carbon nanorods for electromagnetic wave absorption

Letian Huang [a,b], Chunhui Bai [a,b], Jinyu Jia [a,b], Yujin Chen [a,b,c,*], Chunling Zhu [c,*], Xinzhi Ma [d,*], Xiao Zhang [a,b,*]

[a] *Key Laboratory of Photonic Materials and Devices Physics for Oceanic Applications, Ministry of Industry and Information Technology of China, College of Physics and Optoelectronic Engineering, Harbin Engineering University, Harbin 150001, China*

[b] *Key Laboratory of In-Fiber Integrated Optics of Ministry of Education, College of Physics and Optoelectronic Engineering, Harbin Engineering University, Harbin 150001, China*

[c] *College of Materials Science and Chemical Engineering, Harbin Engineering University, Harbin 150001, China*

[d] *Key Laboratory for Photonic and Electronic Bandgap Materials, Ministry of Education, School of Physics and Electronic Engineering, Harbin Normal University, Harbin 150025, China.*

Abstract

Magnetic carbon-based composites exhibited enhanced electromagnetic wave (EMW) absorption performance; however, their fabrications through conventional annealing methods need a relatively long time. Herein, FeCo alloy nanoparticles (NPs)

*Corresponding authors.
E-mail addresses: chenyujin@hrbeu.edu.cn; zhuchunling@hrbeu.edu.cn; maxz@hrbnu.edu.cn; zhangxiaochn@hrbeu.edu.cn

embedded in porous carbon nanorods are synthesized through a rapid Joule heating method within 10 seconds. The ~170-nm-FeCo NPs encapsulated in graphene layers are embedded in porous carbon nanorods with a diameter of around 500 nm. Density functional theory (DFT) calculations and experimental results show that the orbital hybridization of Fe and Co atoms can adjust the d-band center and induce magnetic coupling effects, while the charge redistribution at the interfaces between FeCo alloys and the graphene layers enhances dielectric loss. In addition, the structural features, including porous and one-dimensional structures, synergistically improve EMW absorption performance. Consequently, the optimal FeCo-CNRs achieve an effective absorption bandwidth (EAB) of 6.08 GHz at a matching thickness of only 1.9 mm, outperforming single counterparts and most of the reported magnetic carbon-based absorbers. This work aims to provide a rapid approach for developing magnetic carbon composites for high-performance EMW absorption.

Keywords: Joule heating; magnetic alloy nanoparticles; porous carbon nanorods; electromagnetic wave absorption

1. Introduction

With the widespread deployment of fifth-generation (5G) mobile communication technology, the issues related to electromagnetic radiation become severe. Studies have shown that electromagnetic radiation poses a certain threat to the operation of precision electronic equipment and human health [1-6]. Electromagnetic wave (EMW) absorbing materials, which have the capability to absorb or substantially attenuate EMW energy, play an irreplaceable role in the fields of electronic equipment anti-interference, military stealth coatings, and EM compatibility [7, 8]. Carbon-based materials, distinguished by low density, high dielectric loss, and remarkably stable chemical properties, are considered ideal candidate materials. However, pure carbon materials have low magnetic loss due to their intrinsic non-magnetic property, which limits their further applications [9]. Magnetic materials, to some extent, exhibit higher magnetic loss, but their drawbacks, such as elevated density and diminished stability, significantly impede future application [10].

Combining magnetic materials with carbon materials to construct magnetoelectric composites can achieve magnetoelectric synergy, greatly enhancing impedance matching characteristics and magnetic loss while maintaining dielectric loss [11-14]. Thus, magnetic carbon-based composites have been engineered for EMW absorption. For example, Wen *et al.* prepared Co@S-doped carbon cores and hollow N-doped carbon shells, where the presence of Co NPs promoted magnetoelectric synergy and strengthened EMW absorption performance [15]. Using egg-derived carbon (EDC) as a precursor, Miao *et al.* synthesized EDC@Fe_3O_4 nanocomposites with excellent EMW

absorption performance [16]. The magnetic part caused magnetic loss, while the carbon structure, which had many defects and holes, helped with scattering and energy loss. The cooperative effect between the magnetic Fe_3O_4 NPs and the porous carbon carrier improved impedance matching characteristics, at 2.03 mm, achieving a broad effective absorption bandwidth (EAB) of 5.68 GHz. Su *et al.* prepared a nanocomposite composed of graphene and iron covered with BN on the surface via ball milling [17]. At 1.4 mm, this composite attained a minimum reflection loss (RL_{min}) of -44.53 dB, exhibiting an EAB of 4.40 GHz. Recently, researchers have found that magnetic alloys could further improve EMW absorption performance [18]. By utilizing the interaction between two magnetic metals with strong d-d orbital hybridization [19], the d-band center and charge redistribution can be adjusted, thereby enhancing interface polarization and EMW absorption performance [20]. Meanwhile, the graphite carbon layer catalyzed by magnetic alloys can construct electron mobility pathways, improving conductive loss [21]. However, the synthesis of traditional magnetic alloy-carbon composites typically relies on methods such as ball milling [22], chemical vapor deposition [23], and high-temperature pyrolysis [24], which have drawbacks such as long preparation times, easy growth of magnetic particles, and high defect rates in the carbon carrier [25, 26]. Consequently, there is an imperative necessity to devise an efficient and controlled method for synthesizing magnetic metal alloy-carbon composites.

The Joule heating method, as an emerging rapid thermal processing technology, demonstrates significant advantages over traditional tube furnace heating [27, 28].

Joule heating achieves a sudden local temperature rise within seconds by instantaneously applying ultra-high current at both ends of the sample, converting electrical energy directly into thermal energy through resistance [29]. This method is markedly superior to traditional techniques such as tube furnace pyrolysis, which require several hours to complete thermal treatment. Additionally, traditional heating can partially damage the morphology at high temperatures [30], whereas Joule heating significantly reduces the experimental cycle duration and mitigates adverse reactions via quick cooling [31]. This effectively controls the composition and microstructure of metal alloys, preventing metal aggregation caused by uneven temperatures in traditional methods [32]. For instance, Wang *et al.* employed the Joule heating strategy to prepare Co-loaded carbon absorbers with adjustable impedance matching, achieving a RL_{min} of -46.5 dB at 2.48 mm [28]. Wang *et al.* fabricated honeycomb-structured porous carbon nanofibers containing uniformly dispersed FeCoNiCuMn high-entropy alloy NPs through rapid Joule heating treatment, significantly enhancing conductivity, promoting efficient electron conduction, and improving their EMW absorption performance [33]. Thus, the Joule heating method overcomes the constraints of conventional techniques, offering new possibilities for advanced EMW absorption materials.

Herein, we propose a method for rapid synthesis of composite materials consisted of FeCo alloy NPs embedded in a carbon nanorod framework using joule heating. FeCo precursor nanowires were synthesized via a solvothermal method, and ultrahigh temperatures (1500 ℃) induced by Joule heating were used for instantaneous

processing, achieving the decrease of metal ions and simultaneous graphitization of the carbon carrier. The formation of FeCo alloy particles not only ensures magnetic loss but also catalyzes the graphitization of carbon to construct electronic mobility pathways, enhancing conductive loss. Theoretical calculations indicate that the introduction of FeCo with d-d orbital hybridization can adjust the d-band center. Meanwhile, the charge redistribution between Fe and Co atoms and the carbon support can enhance interface polarizations. As a result, the FeCo-CNRs achieve an EAB of 6.08 GHz at a matching thickness of 1.9 mm, significantly outperforming the single-metal systems in this study. This research introduces a novel method for the construction of EMW absorbing magnetic metal alloy-carbon composite system design materials.

2. Experiment

2.1 Synthesis of FeCo precursor nanowires

According to previously reported literature [34], FeCo precursor (FeCo-pre) nanowires were synthesized using the solvothermal method. Specifically, 0.6 g of nitrilotriacetic acid (NTA), 0.63 g of $FeCl_2 \cdot 4H_2O$ and 0.75 g of $CoCl_2 \cdot 6H_2O$ were dissolved in a mixed solvent system consisting of 27 mL of isopropyl alcohol (IPA) and 13 mL of deionized water. The solution was magnetically stirred for 30 minutes, transferred into a 50 mL Teflon-lined container, and maintained at 180 °C for 6 hours, and cooled naturally to room temperature after the reaction. The samples were centrifuged at 6000 rpm, washed with deionized water and ethanol, and dried in an oven at 60 °C. Finally, the FeCo-pre was obtained.

2.2 Synthesis of FeCo-CNRs

The rapid Joule heating process involved applying high voltage and high current to heat precursor-loaded carbon cloth under an Ar atmosphere. Specifically, 100 mg of FeCo precursor was loaded onto the carbon cloth. The temperature was raised to 1500°C within 1 second, maintained at this temperature for 1 second, and then cooled to room temperature. The total duration of the Joule heating process was less than 10 seconds. The resulting material consisted of FeCo alloy NPs embedded in a carbon nanorod framework (FeCo-CNRs).

2.3 Synthesis of Fe-CNRs and Co-CNRs

The synthesis of Fe and Co precursor (Fe-pre and Co-pre) nanowires follows the same method as above, only changing the metal salts added. The same method was used to make Fe-CNRs and Co-CNRs, only changing the FeCo-pre to Fe-pre and Co-pre, respectively.

2.4 Characterizations

Detailed characterization data, including structural characterizations, electromagnetic formulas, density functional theory (DFT) calculations and radar cross-section (RCS) simulations, are provided in the Supporting Information.

3. Results and discussion

Figure 1 illustrates the synthesis method for FeCo-CNRs. In a mixed solution including IPA and deionized water, metal cations Fe^{2+} and Co^{2+} coordinate with NTA, and then the precursor nanowires (FeCo-pre) are synthesized through a solvothermal reaction. Under an argon atmosphere, the Joule heating apparatus rapidly heats the material from room temperature to 1500°C and then quickly cools it back to room

temperature in 10 seconds. During the heating process, the metal cations in the FeCo-pre are rapidly reduced to form a metal alloy. In the ultrafast high-temperature carbonization process, the high temperature provides sufficient energy for the metal atoms to overcome the lattice displacement energy barrier, and these metal atoms eventually form an alloy phase through mutual diffusion. The carbon in the nanowires serves as the framework for the carbon nanorods, while the magnetic metal NPs facilitate the graphitization of the carbon carrier. Ultimately, the composite materials of FeCo alloy NPs embedded in a carbon nanorod framework were successfully prepared. Similarly, the synthesis of analogous samples, such as Fe-CNRs and Co-CNRs, only required substituting the corresponding metal salts while keeping all other parameters constant.

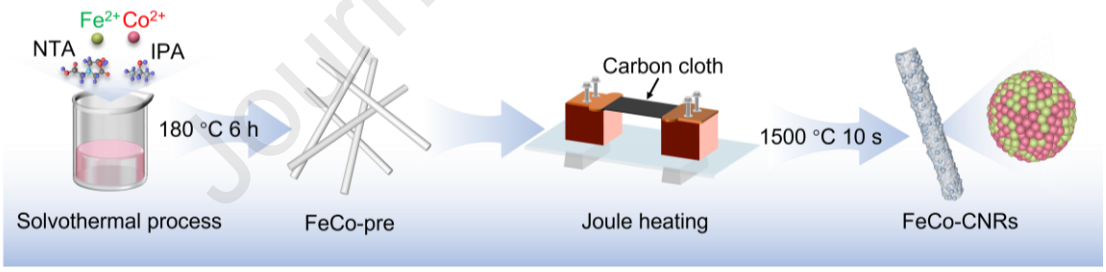

Figure 1. Schematic diagram of the synthesis of FeCo-CNRs.

The surface morphology of the samples was characterized by scanning electron microscopy (SEM). SEM images of Fe-pre, Co-pre, and FeCo-pre exhibit diameters ranging from 100 to 400 nm, while their lengths extend to several tens of micrometers (Figure S1 and Figure 2a). After rapid Joule heating, FeCo-pre transformed into FeCo-CNRs, as shown in Figure 2b, where nanorods were uniformly decorated with FeCo

NPs, exhibiting diameters between 20 and 300 nm (average size: 170 nm). In contrast, the Fe-CNRs and Co-CNRs do not show well-defined particle-carbon skeleton structure compared to FeCo-CNRs (Figure S2). This may be because the FeCo alloy can promote graphitization of carbon materials [35], making the overall FeCo-CNRs structure more stable. Transmission electron microscopy (TEM) was further employed to examine the detailed microstructure and crystal features. Further insights into the microstructure of FeCo-CNRs were gained from TEM images (Figure 2c), which show carbon nanorods with a diameter of approximately 500 nm embedded with FeCo NPs. Owing to the catalytic graphitization property of metals at elevated temperatures [36, 37], a graphene layer at 3.907 nm forms near the FeCo NPs (Figure 2d). The thickness of the graphene layer depends on the size of the FeCo NPs, and TEM images indicate a uniform core-shell structure with FeCo magnetic particles and a dielectric graphite carbon layer. These magnetic NPs establish heterogeneous interfaces with the graphene layer, thereby promoting favorable interfacial polarization [38, 39]. TEM images also reveal the presence of numerous porous structures in the FeCo-CNRs. Additionally, the FeCo magnetic NPs facilitate the formation of graphitic carbon layers, which enhance conduction loss through efficient electron transport pathways [40]. The formation of conductive networks, porous structures and heterogeneous interfaces can enhance conductivity loss and polarization loss, which is beneficial for improving EMW absorption performance [41]. In the high-resolution TEM (HRTEM) images (Figure 2e), the lattice fringes marked as 0.20 nm and 0.34 nm correspond to the (110) crystal plane of the FeCo alloy and the (002) crystal plane of the carbon layer, respectively. The

corresponding fast Fourier transform (FFT) pattern (Figure 2f) illustrates the directions of the (110) and (211) crystal planes of the FeCo alloy, and the (002) crystallographic plane direction of the carbon layer in reciprocal space. High-angle annular dark-field scanning transmission electron microscopy (HAADF-STEM) and its corresponding energy-dispersive X-ray (EDX) elemental mapping analysis show that the material contains Fe, Co, and C elements (Figure 2g). Fe and Co are uniformly scattered within each particle, confirming the formation of FeCo alloy NPs. C is uniformly distributed in the carbon framework. This aligns with the EDX spectrum patterns observed in SEM and TEM images (Figures S3).

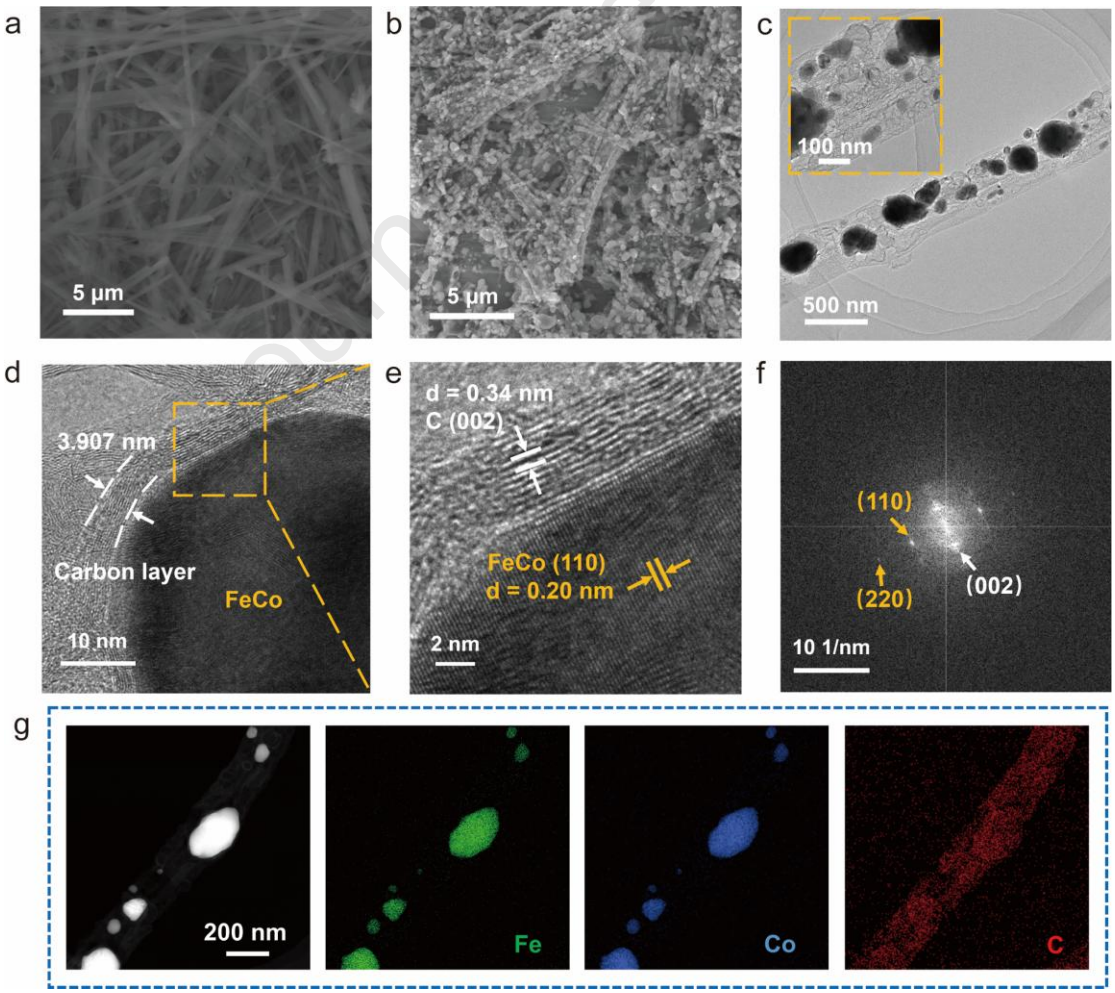

Figure 2. (a) SEM image of FeCo-pre. (b) SEM image, (c) TEM image, (d-e) HRTEM

images with corresponding (f) FTT pattern, (g) HAADF-STEM and the corresponding elemental mappings of FeCo-CNRs.

Figure 3a displays the X-ray diffraction (XRD) pattern of the as-prepared precursor nanowires. Only broad diffraction peaks centered at 26.5° are observed, indicating the amorphous nature of those precursor nanowires. The XRD patterns of the as-synthesized Fe-CNRs, Co-CNRs, and FeCo-CNRs display broad diffraction peaks of the (002) plane of graphitic carbon (Figure 3b). The FeCo-CNRs exhibit diffraction peaks at 45.077°, 65.651°, and 83.198°, which were indexed to the (110), (200), and (211) crystal planes of a body-centered cubic (BCC) structure of FeCo alloy (PDF#04-003-3891). These features are consistent with the (110) and (200) crystal planes observed in the FTT pattern (Figure 2f). The Fe-CNRs exhibit diffraction peaks at 43.380°, 50.524°, 74.245°, 90.095°, and 95.320°, which are consistent with the (111), (200), (220), (311), and (222) crystal planes of the face-centered cubic (FCC) structure of Fe (PDF#98-000-0258). The diffraction peaks at 44.674°, 65.022°, and 82.334° match the (110), (200), and (211) crystal planes of the BCC structure of Fe (PDF#00-006-0696). According to the fitting results of the XRD diffraction peaks, it can be determined that in Fe-CNRs, the BCC phase of Fe accounts for ~56.8 wt.%, while the FCC phase accounts for ~43.2 wt.% (Table S1). Both FCC and BCC phases coexist in the Fe-CNRs sample [42], possibly due to the extremely short duration of Joule heating, which results in a portion of the FCC phase not transforming into the BCC phase. The Co-CNRs exhibit diffraction peaks at 43.948°, 51.198°, 75.329°, 91.534°, and 96.898°, corresponding to the (111), (200), (220), (311), and (222) crystal planes of the FCC

structure of the Co (PDF#04-004-7807), respectively. As illustrated in Figure 3c, Raman spectroscopy is used to assess the degree of graphitization and carbon defects in the materials [43]. The Fe-CNRs, Co-CNRs, and FeCo-CNRs all show D and G bands near 1342 and 1580 cm^{-1}. The intensity ratio of the D to G bands (I_D/I_G) can reflect the defect level and graphitization degree [44, 45]. The I_D/I_G values for Fe-CNRs, Co-CNRs, and FeCo-CNRs are 0.27, 0.37, and 0.13, respectively, indicating that FeCo alloy NPs significantly enhance the graphitization degree of FeCo-CNRs [46], which facilitates enhanced electrical conductivity losses, thereby potentially tuning EMW absorption. X-ray photoelectron spectroscopy (XPS) was employed to characterize the valence states and elemental composition. Figure 3d verifies the existence of C, O, Fe, and Co components. Figure 3e compares the Fe 2p peaks of Fe-CNRs and FeCo-CNRs, showing that the Fe $2p_{1/2}$ (724.1 eV) and Fe $2p_{3/2}$ (712.8 eV) peaks of FeCo-CNRs shift to higher binding energies compared to the Fe $2p_{1/2}$ (723.9 eV) and Fe $2p_{3/2}$ (711.9 eV) of Fe-CNRs. Figure 3f compares the Co 2p peaks of Co-CNRs and FeCo-CNRs. The Co $2p_{1/2}$ (797.1 eV) and Co $2p_{3/2}$ (781.8 eV) peaks of FeCo-CNRs shift to higher binding energies compared to the Co $2p_{1/2}$ (796.2 eV) and Co $2p_{3/2}$ (779.6 eV) peaks of Co-CNRs. Theoretically, Co should attract electrons from Fe, causing the binding energy of Fe to increase and that of Co to decrease. However, an increase in binding energies for both elements was observed, indicating stronger interactions among the FeCo alloy particles and the carbon carrier, which facilitates interfacial polarization loss. Additionally, the high-resolution C 1s XPS spectrum (Figure 3g) can be deconvoluted into four distinct components, which are attributed to different chemical bonding states:

C−C, C−N, C−O, and C=O. The presence of C−O indicates oxygen-containing functional groups in the amorphous carbon. The polar groups C−N and C−O/C=O can serve as dipolar polarization centers [19], facilitating polarization loss. The disappearance of the C=O group in FeCo-CNRs results from the coexistence of Fe and Co forming intermetallic electronic coupling, enhancing the reduction capability of system. During the synthesis process, the FeCo alloy may act as a catalyst to promote the conversion of C=O to C−C/C−O, more effectively facilitating the carbon graphitization at high synthesis temperatures, consistent with the Raman spectra (Figure 3c). Based on the structural characterization results, the microstructure of the FeCo precursor nanowires underwent a significant evolution. During the joule heating process, the organic ligands in the precursor rapidly decomposed, with a portion forming gases that escaped and another portion being carbonized, thus resulting in the formation of porous-structured nanorods. On the other hand, the Fe and Co ions were reduced via carbothermal reduction, forming FeCo alloy NPs. These alloy particles acted as catalysts, promoting the graphitization of the surrounding carbon materials and forming a graphitic coating layer on FeCo particles.

In this work, due to the presence of magnetic NPs in the prepared samples, the magnetism may influence their EMW absorption capabilities. The intrinsic magnetism of the materials was measured using a vibrating sample magnetometer (VSM) (Figures 3h-i). According to the Stoner-Wohlfarth theory, materials with high saturation magnetization (M_S) and suitable coercivity (H_C) can have better magnetic permeability, thereby improving their ability to store and dissipate magnetic energy [47]. The M_S

values for Fe-CNRs, Co-CNRs, and FeCo-CNRs are 85.121 emu/g, 94.035 emu/g, and 66.657 emu/g, respectively, with corresponding H_C values of 44.73 Oe, 153.68 Oe, and 77.37 Oe. The moderate H_C values of FeCo-CNRs can optimize the complex magnetic permeability, reduce EMW reflection, and improve absorption efficiency. However, due to slight differences in the content of magnetic NPs in the materials and the carbon layer coating on the particle surfaces, the magnetism has little effect on their EMW absorption performance.

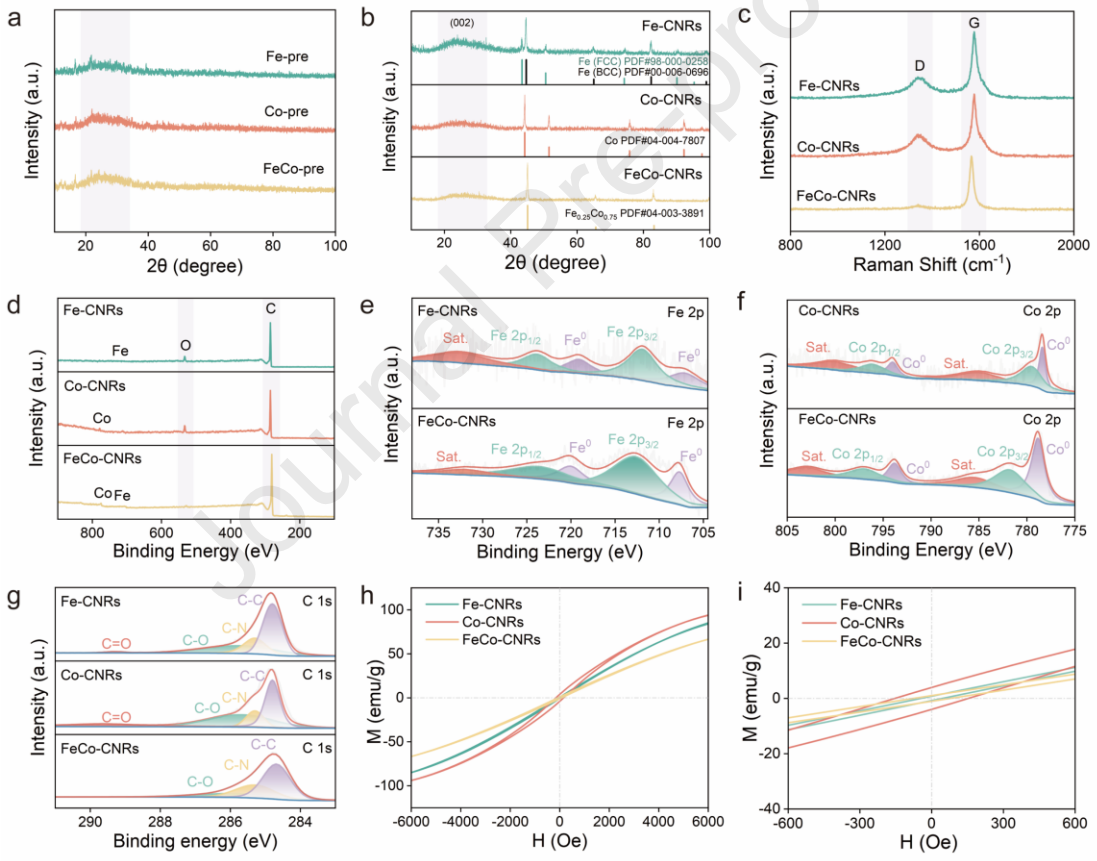

Figure 3. XRD patterns of (a) Fe, Co and FeCo-pre, (b) Fe, Co and FeCo-CNRs. (c) Raman spectra of Fe, Co and FeCo-CNRs. (d) The survey XPS spectra of FeCo-CNRs. The (e) Fe 2p, (f) Co 2p and (g) C 1s core level XPS spectra of FeCo-CNRs. (h-i) Magnetization hysteresis loops of Fe, Co and FeCo-CNRs.

For evaluating EMW absorption performance, Reflection loss (*RL*) is an essential metric [48]. The EAB represents the frequency region in which the *RL* values remain lower than -10 dB, corresponding to 90% attenuation of incident EMW energy [49]. Regarding *RL*, FeCo-CNRs achieve a RL_{min} values of -49.56 dB at 3.7 mm (Figure 4a), which is nearly 6 times and 4.5 times larger than the RL_{min} values of Fe-CNRs (-8.42 dB, Figure 4b) and Co-CNRs (-11.03 dB, Figure 4c), respectively. This indicates that the bimetallic synergistic effect markedly improves the EMW absorption performance of FeCo-CNRs. More importantly, the EAB of FeCo-CNRs reaches 6.08 GHz (covering the C to X band, Figure 4d), far exceeding and the Fe-CNRs of 0 GHz (Figure 4e) and the Co-CNRs of 0.88 GHz (Figure 4f). This clearly demonstrates the inherent limitations of single metal components in broadband absorption performance and confirms the influence of the synergistic effect of Fe and Co bimetals, the degree of carbon graphitization, and the porous morphology on EMW absorption performance [50]. Performance evaluations were conducted on FeCo-CNRs with different thicknesses (Figure 4g). FeCo-CNRs exhibit exceptional EAB performance (>5.84 GHz) within the 1.8-2.2 mm thickness range. Comparative analysis reveals that FeCo-CNRs demonstrate superior EAB relative to conventional carbon-based EMW absorbers documented in literature (Figure 4h, Table S2). Moreover, the attenuation coefficient (α) employing to assess the absorption efficiency of EMW [51]. A higher α value indicates a faster attenuation rate of the incident EMW. The α value of FeCo-CNRs ranges from 64.6 to 374.3, which is higher than that of all other samples (Figure S4), indicating the fastest attenuation rate of EMW.

The impedance matching value (*Mz*) is an essential metric for affecting EMW absorption performance [52]. Generally, when the absorber has an ideal *Mz*, it significantly indicates that more EMW can enter the absorber [53]. Figures S5 show the impedance matching characteristics of Fe-CNRs, Co-CNRs, and FeCo-CNRs. The *Mz* of FeCo-CNRs is closer to 1, resulting in excellent EMW absorption performance, whereas the poorer impedance matching of Fe-CNRs and Co-CNRs reflects their weaker performance, confirming the limitations of single metal components in EMW absorption performance.

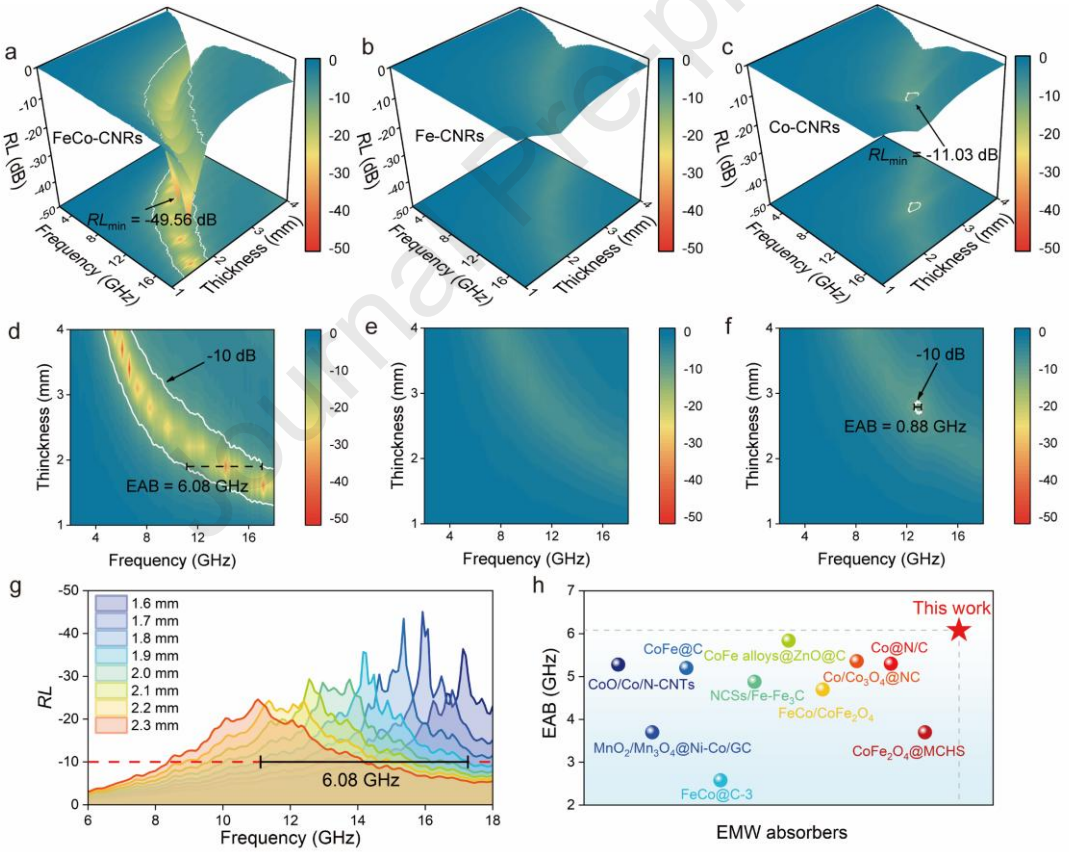

Figure 4. 3D *RL* mappings and corresponding 2D contour plots of (a and d) FeCo-CNRs, (b and e) Fe-CNRs and (c and f) Co-CNRs. (g) 2D of the reflection loss curves of FeCo-CNRs at the range from 1.6 to 2.3 mm. (h) The EAB values of FeCo-CNRs in

comparison to previous reports.

To clarify the mechanism behind the EMW absorption characteristics of FeCo-CNRs. Figure 5 illustrates the dielectric and magnetic loss characteristics of Fe-CNRs, Co-CNRs, and FeCo-CNRs within the 2-18 GHz range. The EM parameters of the absorbers include complex permittivity ($\varepsilon_r = \varepsilon' - j\varepsilon''$) and complex permeability ($\mu_r = \mu' - j\mu''$), where ε' and μ' denote the ability to store EM energy, while ε'' and μ'' denote the ability to dissipate EM energy [54, 55]. As shown in Figure 5a, the ε' of FeCo-CNRs demonstrates a significant advantage in the 2-18 GHz band, with an initial value reaching 10.78 and remaining above 7 as the frequency increases. However, the ε' values of the single metal systems (Fe-CNRs and Co-CNRs) are all below 7, indicating that bimetallic FeCo-CNRs facilitate the EM energy storage [56]. Figure 5b illustrates the curve of ε'', and from the overall trend, the ε'' values of Fe-CNRs and Co-CNRs are both below 1, indicating that their dielectric loss capabilities are limited. In contrast, the ε'' values of FeCo-CNRs remain between 2.78 and 4.31, demonstrating a more balanced broadband dielectric loss characteristic [57]. This phenomenon may be explained by the synergistic effect between Fe and Co atoms in the CNRs [58]. From the perspective of the average dielectric loss tangent value ($\tan\delta_e = \varepsilon''/\varepsilon'$, Figure 5c), FeCo-CNRs, Fe-CNRs, and Co-CNRs are 0.37, 0.07, and 0.11, respectively. The values of FeCo-CNRs markedly exceed those of two other samples, indicating that the FeCo-CNRs have enhanced dielectric loss capability compared to Fe-CNRs and Co-CNRs [59]. As shown in Figure S6, Cole-Cole curves of FeCo-CNRs display a larger semicircular arc accompanied by an extended tail region, suggesting that polarization

and conductivity loss significantly influence the dielectric loss mechanisms [60, 61].

Magnetic losses mainly include exchange resonance, natural resonance, eddy current loss, domain wall resonance, and hysteresis loss [62]. Due to the occurrence of domain wall resonance in the low-frequency region, these can often be neglected [63]. The value of μ' remains comparatively constant, with the μ' of FeCo-CNRs averaging 0.28 more than that of the other two samples within the 2-18 GHz range (Figure 5d). It indicates that the magnetic moment coupling effect of the bimetallic component effectively enhances the material's static magnetic energy storage capacity [64, 65]. As seen in Figure 5e, FeCo-CNRs exhibit larger μ'' values than Fe-CNRs and Co-CNRs, indicating their stronger magnetic loss ability, confirmed by the magnetic loss tangent values ($\tan\delta_m = \mu''/\mu'$, Figure 5f) [66]. Eddy current loss was evaluated by the coefficient C_0 ($C_0 = \mu''(\mu')^{-2}f^{-1}$). As seen in Figure S7, there are strong vibrations in the C_0 curves within the 2-18 GHz range suggests that the eddy current loss was not significant in the three samples. Notably, for all the samples, a discernible peak at approximately 2.0 GHz is evident in Figure 5f, which is attributable to the natural resonance. However, another broad peak centered at 10.4 GHz is presented in the FeCo-CNRs, while absent in the Fe-CNRs and Co-CNRs. According to the previous reports [67], the peak at a high frequency comes from exchange resonance. Therefore, the magnetic loss of FeCo-CNRs is enhanced due to the additional exchange resonances that may be caused by the magnetic coupling effect of FeCo alloys.

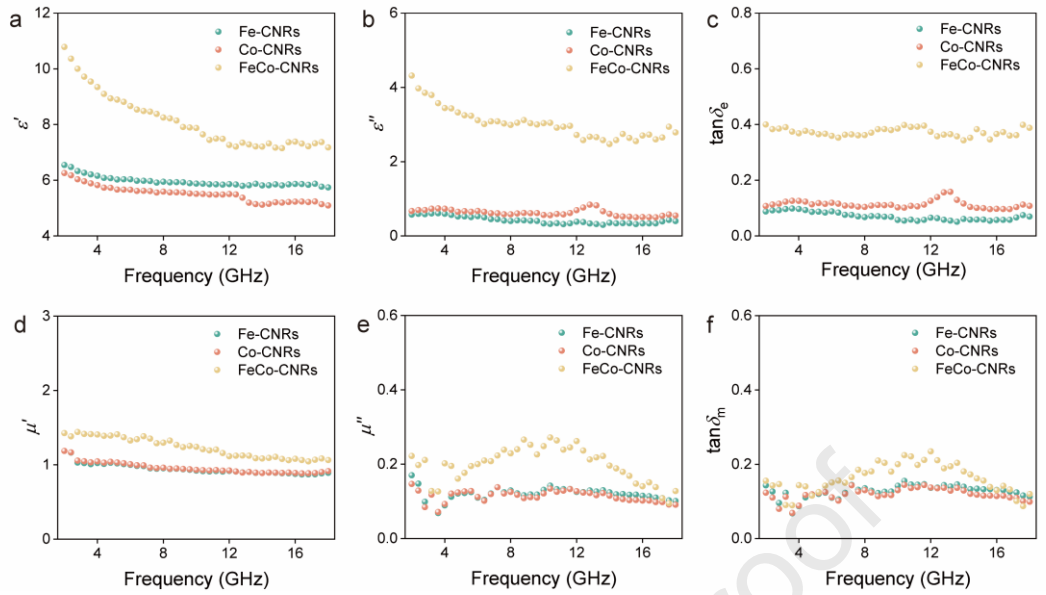

Figure 5. (a) ε'–f, (b) ε''–f, (c) tanδ_e–f, (d) μ'–f, (e) μ''–f and (f) tanδ_m–f curves of Fe-CNRs, Co-CNRs, and FeCo-CNRs.

To further elucidate the mechanism of EMW absorption, we compared electronic characteristics of FeCo/C, Fe/C (FCC), Fe/C (BCC), and Co/C, and pure carbon materials by analyzing the density of states (DOS) through DFT calculations (Figures 6a). It is clear that FeCo/C, Fe/C, and Co/C display pronounced electronic state peaks near the Fermi level, with their total density of states in the energy range of -5.0 to 2.6 eV being significantly higher than that of the pure carbon system. Notably, the strong contribution of the d orbitals near the Fermi surface indicates that the introduction of metal atoms markedly enhances the electronic activity. From the d-band center (Table S3), it can be observed that the d-band of FeCo/C is positioned between those of Fe/C and Co/C, approximately at -1.002 eV, suggesting a certain electronic interaction between Fe and Co. The orbital hybridization effect between d electrons in metals and p electrons in carbon near the Fermi level is stronger. This leads to more electrons

occupying higher energy levels, effectively increasing the electron density near the center of the d-band and promoting electron hopping and rearrangement. The charge differential density maps (Figure 6b) reveal the charge redistribution phenomenon between metal particles and the carbon substrate through the accumulation of red (dissipation of blue) regions. The red regions accumulate electrons at the interface, reflecting the interfacial polarization characteristics of metal and carbon [68]. Mulliken population analysis (Figure 6c) more intuitively presents the atomic arrangement differences in the metal/carbon composite system, showing that electrons predominantly transfer from Fe/Co atoms to the carbon substrate, forming a stronger dipole system that enhances the system's relaxation response to EMW. By comparing the dipole moments of the systems [69, 70], Figure 6d shows that the interfacial dipole strength of the FeCo/C system (17.23 Debye) is higher than that of the Fe/C (17.02 Debye) and Co/C (14.31 Debye) systems. The dipole enhancement effect partially arises from the synergistic effect of the Fe-Co bimetallic system, further indicating a positive impact on polarization loss.

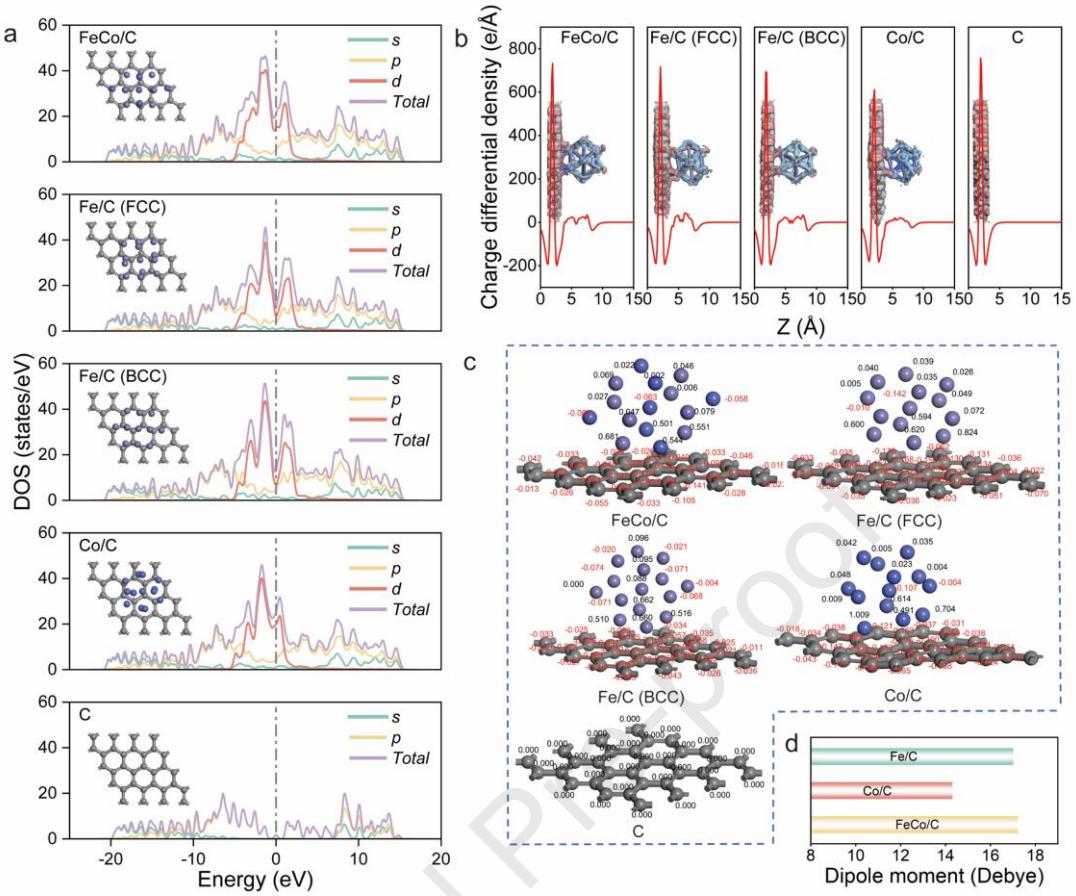

Figure 6. DOS of (a) FeCo/C, Fe/C (FCC), Fe/C (BCC), Co/C, and C models. (b) The charge differential density of FeCo/C, Fe/C (FCC), Fe/C (BCC), Co/C, and C heterointerface. (c) Population analysis of FeCo/C, Fe/C (FCC), Fe/C (BCC), Co/C, and C. (d) The dipole moments of Fe/C, Co/C and FeCo/C.

Figure 7 briefly outlines the EMW absorption mechanism of FeCo-CNRs. First, the carbon nanorods and embedded FeCo NPs in FeCo-CNRs contribute to both magnetic and dielectric loss. Second, the surface topography and porous structure facilitate the transmission path of EMW and optimization of the impedance matching. Carbon nanorods also promote conductive loss through the generation of a conductive network in the carrier. Additionally, the carbon defects can serve as polarization centers, inducing dipole polarization and associated dielectric relaxation under alternating EM

fields. The combination of alloy particles and carbon materials in FeCo-CNRs creates interface regions, and the rich heterogeneous interfaces result in space charge accumulation, triggering strong interfacial polarization. Finally, due to the introduction of magnetic components in FeCo-CNRs, under the influence of alternating electric fields, strong magnetic loss capability is induced through natural and exchange resonances. The EMW attenuation capability is influenced by both magnetic and dielectric loss, and the combined effect of these mechanisms ultimately optimizes impedance matching to elevate the EMW absorption capability of FeCo-CNRs.

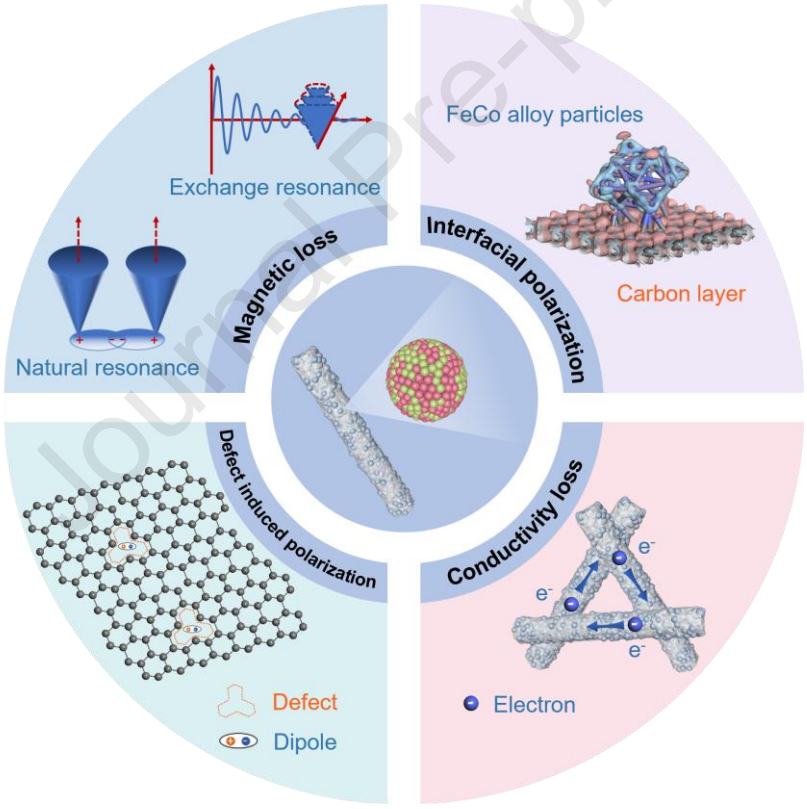

Figure 7. EMW absorption mechanism of FeCo-CNRs.

To assess the EMW absorption capability of Fe-CNRs, Co-CNRs and FeCo-CNRs, simulations were performed. The three-dimensional RCS modeling findings demonstrate that the FeCo-CNRs have considerable advantages in EMW regulation.

Figure 8a shows the variation in detection angles from 0° to 180° in the sample's 3D radar map. Compared to Fe-CNRs and Co-CNRs, the radar scattering signal of FeCo-CNRs is significantly reduced, indicating that FeCo-CNRs can dissipate more EM energy [71]. This spatial scattering characteristic is further verified in the two-dimensional RCS curve (Figure 8b): the oscillation amplitude of FeCo-CNRs is significantly higher than that of Fe-CNRs and Co-CNRs compared to the PEC substrate. The RCS reduction analysis (Figure 8c) reveals the synergistic effect of the material system, with FeCo-CNRs showing a greater reduction effect in different scattering directions compared to single-metal systems (Fe-CNRs, Co-CNRs). The consistency between RCS simulation and EMW absorption characteristics further illustrates the significant advantages of bimetallic systems over single-metal systems, indicating that bimetal-carbon composites have greater application potential.

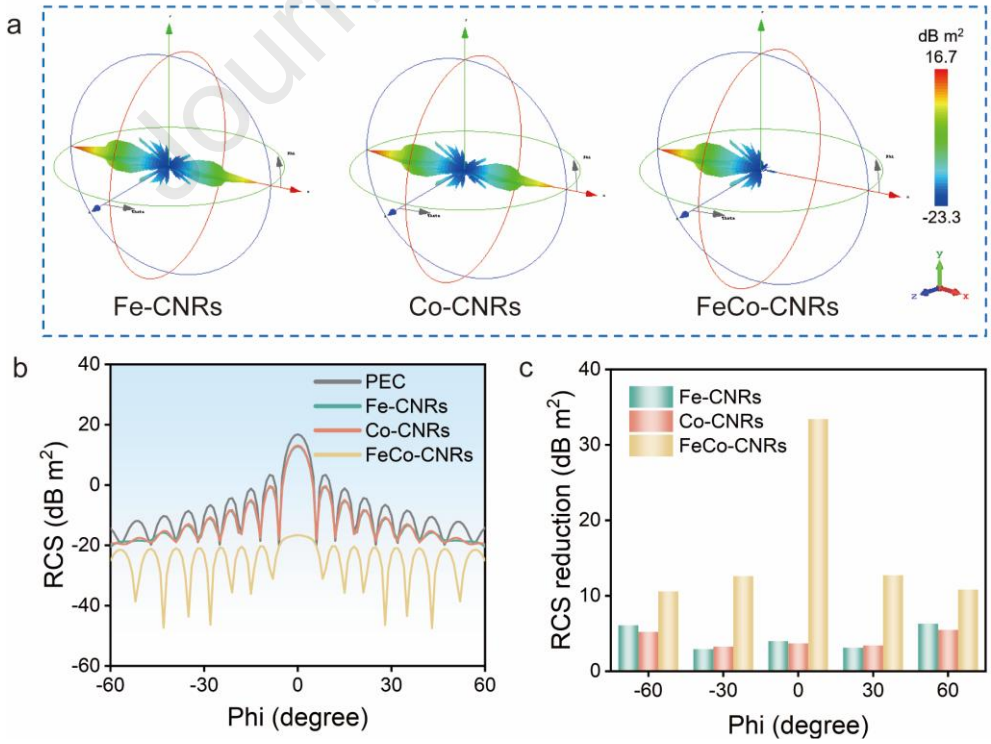

Figure 8. 3D RCS simulations for (a) Fe-CNRs, Co-CNRs and FeCo-CNRs. (b) RCS

simulated curves of Fe-CNRs, Co-CNRs and FeCo-CNRs. (c) RCS values obtained by deducting composite from PEC of Fe-CNRs, Co-CNRs, FeCo-CNR.

In addition, to investigate the impact of different synthesis temperatures and Fe and Co molar ratios on FeCo-CNRs. Figure S8 shows the FeCo-CNRs at different synthesis temperatures and metal molar ratios. The SEM image reveals that the carbon framework is not formed well in the sample obtained at 1300 °C (Figure S8a). At 1700 ℃, the carbon framework in the obtained sample is broken, leading to larger bimetal particle sizes (Figure S8b). When the Fe to Co molar ratio was modified to 1: 2 (Figure S8c), the obtained sample exhibited irregular morphology. When the Fe to Co molar ratio was changed to 2: 1 (Figure S8d), the obtained sample shows uniform one-dimensional morphology composed of porous metal particle embedded in carbon nanorods. Figure S9a displays the XRD patterns of FeCo-CNRs synthesized at various temperatures. The samples obtained at several temperatures exhibit little difference in their components. The samples obtained at the Fe to Co molar ratio of 1: 1 and 2: 1 have similar crystal phase components (Figure S9b). However, an additional FCC structure of Co is formed in the sample with an Fe to Co molar ratio of 1: 2 (Figure S9b), which is due to the higher amount of Co than Fe in the precursor. Except for the sample obtained at 1700 ℃, the EAB values of all other samples exceed 5.2 GHz (Figure S10), indicating that the synthesis conditions for our magnetic carbon absorbers are widely adjustable. Figure S11 shows the EAB and *RL* values of all synthesized samples. It can be seen more intuitively that the optimal temperature and the ratio of Fe to Co are 1500 ℃ and 1: 1, respectively.

4. Conclusion

In conclusion, we develop a rapid Joule heating method to synthesize FeCo alloy NPs embedded in porous carbon within 10 seconds. At 1.9 mm, the as-prepared FeCo-CNRs achieved an EAB of 6.08 GHz, significantly outperforming single-metal counterparts and most of the reported magnetic carbon-based absorbers. Experimental results and theoretical calculations indicate that the enhanced EMW absorption performance of FeCo-CNRs is attributed to the interfacial polarization loss induced by the interfaces between FeCo alloys and the graphene coating layer, and additional exchange resonance came from the magnetic coupling effect of FeCo alloys as well as structural features such as porous and one-dimensional shape. This research presents a novel method for synthesizing effective EMW absorbers.

CRediT authorship contribution statement

Letian Huang: Writing – original draft, Formal analysis, Data curation. **Chunhui Bai:** Data curation**. Jinyu Jia:** Investigation**. Yujin Chen:** Writing – review & editing, Supervision. **Chunlin Zhu:** Writing – review & editing, Resources. **Xinzhi Ma:** Writing – review & editing. **Xiao Zhang:** Writing – review & editing, Supervision.

Declaration of competing interest

The authors declare that they have no known competing financial interests or personal relationships that could have appeared to influence the work reported in this paper.

Acknowledgement

We thank the National Natural Science Foundation of China (Grant No. 52372283),

the General Program of Postdoctoral Science Foundation of China (Grant No. 2023M740891), and the Basic Research Support Program for Excellent Youth Teachers of Education Department of Heilongjiang Province of China (Grant No. YQJH2023282).

References

[1] J. Shu, W. Cao, M. Cao, Diverse metal-organic framework architectures for electromagnetic absorbers and shielding, Adv. Funct. Mater. 31 (2021) 2100470. https://doi.org/10.1002/adfm.202100470.

[2] Z. Yan, L. Wang, Y. Du, G. Chen, Y. Wu, L. Yang, et al., Local charge regulation in selenides via high-entropy engineering to boost electromagnetic wave absorption, Adv. Funct. Mater. 35 (2025) 2422787. https://doi.org/10.1002/adfm.202422787.

[3] L. Kong, S. Luo, G. Zhang, H. Xu, T. Wang, J. Huang, et al., Interfacial polarization dominant CNTs/PyC hollow microspheres as a lightweight electromagnetic wave absorbing material, Carbon 193 (2022) 216-229. https://doi.org/10.1016/j.carbon.2022.03.016.

[4] C. Han, Q. Zheng, K. Xiang, M. Zhang, M. Cao, Self-assembly of one-dimensional cobalt-carbon to turn dielectric properties for electromagnetic attenuation, Carbon 236 (2025) 120103. https://doi.org/10.1016/j.carbon.2025.120103.

[5] J. Su, X. Zhang, Z. Ma, X. Xu, J. Xu, Y. Chen, Construction of Fe_3C@N-doped graphene layers yolk-shelled nanoparticles on the graphene sheets for high-efficient electromagnetic wave absorption, Carbon 229 (2024) 119448. https://doi.org/10.1016/j.carbon.2024.119448.

[6] Q. Yang, J. Sun, Y. Gao, Y. Lu, Z. Shen, L. Ma, et al., Integrated design and performance of microwave absorbing-mechanical load bearing: metasurface aramid unidirectional cloth composites based on PEDOT: PSS conductive ink, Adv. Compos. Hybrid Mater. 8 (2025) 250. https://doi.org/10.1007/s42114-025-01323-z.

[7] Z. Gao, A. Iqbal, T. Hassan, S. Hui, H. Wu, C. Koo, Tailoring built-in electric field in a self-assembled zeolitic imidazolate framework/MXene nanocomposites for microwave absorption, Adv. Mater. 36 (2024) 2311411. https://doi.org/10.1002/adma.202311411.

[8] H. Guan, J. Zong, M. Wang, H. Zhai, J. Yuan, M. Cao, Facile design and enhanced interface polarization of CoFe-PBA/MXene towards microwave absorption, EMI shielding and energy storage, Carbon 226 (2024) 119239. https://doi.org/10.1016/j.carbon.2024.119239.

[9] X. Xiong, H. Zhang, H. Lv, L. Yang, G. Liang, J. Zhang, et al., Recent progress in carbon-based materials and loss mechanisms for electromagnetic wave absorption, Carbon 219 (2024) 118834. https://doi.org/10.1016/j.carbon.2024.118834.

[10] J. Xu, Z. Ma, P. Yang, C. Zhu, Y. Chen, 3D hierarchically ordered porous carbon frameworks/Co nanoparticles for Broadening electromagnetic wave absorption bandwidth, Carbon 233 (2025) 119916. https://doi.org/10.1016/j.carbon.2024.119916.

[11] X. Jing, Z. Li, Z. Chen, Z. Li, C. Qin, H. Gong, Effect of praseodymium valence change on the structure, magnetic, and microwave absorbing properties of M-type strontium ferrite: the mechanism of influence of citric acid dosage and calcination temperature, Mater. Today Chem. 30 (2023) 101537. https://doi.org/10.1016/j.mtchem.2023.101537.

[12] X. Wang, F. You, X. Wen, K. Wang, G. Tong, W. Wu, Doping $Ce(OH)CO_3$ laminated dendrites with Fe, Co and Ni for defect steered wide-frequency microwave absorption, Chem. Eng. J. 445 (2022) 136431.

https://doi.org/10.1016/j.cej.2022.136431.

[13] L. Liang, W. Gu, Y. Wu, B. Zhang, G. Wang, Y. Yang, et al., Heterointerface engineering in electromagnetic absorbers: new insights and opportunities, Adv. Mater. 34 (2022) 2106195. https://doi.org/10.1002/adma.202106195.

[14] Y. Sun, Y. Shi, X. Zhang, F. Cao, L. Huang, Y. Chen, Pb single-atoms on nitrogen-doped graphene hollow spheres for electromagnetic wave absorption, Carbon 240 (2025) 120352. https://doi.org/10.1016/j.carbon.2025.120352.

[15] B. Wen, H. Yang, Y. Lin, L. Ma, Y. Qiu, F. Hu, et al., Synthesis of core-shell Co@S-doped carbon@ mesoporous N-doped carbon nanosheets with a hierarchically porous structure for strong electromagnetic wave absorption, J. Mater. Chem. A 9 (2021) 3567-3575. https://doi.org/10.1039/D0TA09393A.

[16] Y. Miao, M. Zhang, Q. Liu, T. Xi, Y. Liu, Y. Wang, et al., Egg derived porous carbon decorated with Fe_3O_4 nanorods for high efficiency electromagnetic wave absorption, Carbon 235 (2025) 120076. https://doi.org/10.1016/j.carbon.2025.120076.

[17] Q. Su, D. Liu, C. Wang, L. Xia, X. Huang, B. Zhong, Graphene/BN/Fe/BN nanocomposites for highly efficient electromagnetic wave absorption, ACS Appl. Nano Mater. 5 (2022) 15902-15913. https://doi.org/10.1021/acsanm.2c04129.

[18] X. Du, L. Zhang, C. Guo, G. Liu, H. Yuan, Y. Li, et al., FeCo/graphene nanocomposites for applications as electromagnetic wave-absorbing materials, ACS Appl. Nano Mater. 5 (2022) 18730-18741. https://doi.org/10.1021/acsanm.2c04497.

[19] Y. Wang, W. Zhong, S. Zhang, X. Zhang, C. Zhu, X. Zhang, et al., Pearl necklace-like CoMn-based nanostructures derived from metal-organic frames for enhanced

electromagnetic wave absorption, Carbon 188 (2022) 254-264. https://doi.org/10.1016/j.carbon.2021.12.030.

[20] Z. Zhao, J. Sun, X. Li, S. Qin, C. Li, Z. Zhang, et al., Engineering active and robust alloy-based electrocatalyst by rapid Joule-heating toward ampere-level hydrogen evolution, Nat. Commun. 15 (2024) 7475. https://doi.org/10.1038/s41467-024-51976-5.

[21] M. Huang, B. Li, Y. Qian, L. Wang, H. Zhang, C. Yang, et al., MOFs-derived strategy and ternary alloys regulation in flower-like magnetic-carbon microspheres with broadband electromagnetic wave absorption, Nano-Micro Lett. 16 (2024) 245. https://doi.org/10.1007/s40820-024-01416-2.

[22] Y. Gong, Z. Yang, X. Wei, S. Song, S. Ma, Synthesis and electromagnetic wave absorbing properties of high-entropy metal diboride-silicon carbide composite powders, J. Mater. Sci. 57 (2022) 9218-9230. https://doi.org/10.1007/s10853-022-07238-0.

[23] G. Ma, Y. Yan, Y. Feng, K. Zhang, B. Gao, J. Weng, et al., Multifunctional carbon nanotube arrays on kapok-derived carbon microtube composites for efficient electromagnetic wave absorption and Cu(II) removal, Chem. Eng. J. 500 (2024) 157373. https://doi.org/10.1016/j.cej.2024.157373.

[24] X. Zhang, Z. Zhao, J. Xu, Q. Ouyang, C. Zhu, X. Zhang, et al., N-doped carbon nanotube arrays on reduced graphene oxide as multifunctional materials for energy devices and absorption of electromagnetic wave, Carbon 177 (2021) 216-225. https://doi.org/10.1016/j.carbon.2021.02.085.

[25] Y. Chen, K. Fu, S. Zhu, W. Luo, Y. Wang, Y. Li, et al., Reduced graphene oxide

films with ultrahigh conductivity as Li-ion battery current collectors, Nano Lett. 16 (2016) 3616-3623. https://doi.org/10.1021/acs.nanolett.6b00743.

[26] J. Tang, Y. Gao, T. Li, R. Qin, Q. Qi, F. Meng, Thermoresistive network in phase-transition hydrogel: achieving on/off switchable electromagnetic interference shielding, Adv. Funct. Materials (2025) 2504959. https://doi.org/10.1002/adfm.202504959.

[27] H. Wang, N. Makowski, Y. Ma, X. Fan, S. Maclean, J. Lipton, et al., Metallic glass nanoparticles synthesized via flash Joule heating, ACS Nano 19 (2025) 19806-19817. https://doi.org/10.1021/acsnano.5c02173.

[28] X. Wang, Z. Wang, D. Xi, J. Li, X. Li, X. Bai, et al., Tunable impedance of cobalt loaded carbon for wide-range electromagnetic wave absorption, Small 20 (2024) 2308970. https://doi.org/10.1002/smll.202308970.

[29] B. Deng, Z. Wu, E. Feng, L. Ma, Z. Wang, J. Chen, et al., Coupling amorphization and compositional optimization of ternary metal phosphides toward high-performance electrocatalytic hydrogen production, J. Am. Chem. Soc. 147 (2025) 16129-16140. https://doi.org/10.1021/jacs.5c00071.

[30] N. Chen, J. Jiang, C. Xu, Y. Yuan, Y. Gong, L. Zhen, Co_7Fe_3 and Co_7Fe_3@SiO_2 nanospheres with tunable diameters for high-performance electromagnetic wave absorption, ACS Appl. Mater. Interfaces 9 (2017) 21933-21941. https://doi.org/10.1021/acsami.7b03907.

[31] W. Chen, J. Li, Z. Wang, W. Algozeeb, D. Luong, C. Kittrell, et al., Ultrafast and controllable phase evolution by flash Joule heating, ACS Nano 15 (2021) 11158-11167. https://doi.org/10.1021/acsnano.1c03536.

[32] L. Wang, L. Yang, X. Zhao, H. Ma, B. Pang, L. Duan, et al., Using CrN_4 moiety to weaken the dissociation barrier of hydroxyl on adjacent single iron atom for efficient oxygen reduction, Energy Storage Mater. 74 (2025) 103927. https://doi.org/10.1016/j.ensm.2024.103927.

[33] S. Wang, Q. Liu, S. Li, F. Huang, H. Zhang, Joule-heating-driven synthesis of a honeycomb-like porous carbon nanofiber/high entropy alloy composite as an ultralightweight electromagnetic wave absorber, ACS Nano 18 (2024) 5040-5050. https://doi.org/10.1021/acsnano.3c11408.

[34] Y. Wang, B. Suo, Y. Shi, H. Yuan, C. Zhu, Y. Chen, General fabrication of 3D hierarchically structured bamboo-like nitrogen-doped carbon nanotube arrays on 1D nitrogen-doped carbon skeletons for highly efficient electromagnetic wave energy attenuation, ACS Appl. Mater. Interfaces 12 (2020) 40692-40701. https://doi.org/10.1021/acsami.0c12413.

[35] X. Xu, J. Xie, B. Liu, R. Wang, M. Liu, J. Zhang, et al., PBA-derived FeCo alloy with core-shell structure embedded in 2D N-doped ultrathin carbon sheets as a bifunctional catalyst for rechargeable Zn-air batteries, Appl. Catal. B Environ. 316 (2022) 121687. https://doi.org/10.1016/j.apcatb.2022.121687.

[36] S. Li, X. Han, W. Song, Z. Wang, Y. Zhu, S. Jiao, Nickel-promoted electrocatalytic graphitization of biochars for energy storage: mechanistic understanding using multi-scale approaches, Angew. Chem. Int. Ed. 62 (2023) e202301985. https://doi.org/10.1002/anie.202301985.

[37] F. Wang, Y. Liu, R. Feng, X. Wang, X. Han, Y. Du, A “Win-Win” strategy to

modify Co/C foam with carbon microspheres for enhanced dielectric loss and microwave absorption characteristics, Small 19 (2023) 2303597. https://doi.org/10.1002/smll.202303597.

[38] X. Wang, X. Lv, R. Zhang, X. Yang, R. Dai, W. You, et al., Dimensional self-assembled magnetic coupling via embedding ferromagnetic nanoparticles in multi-channel fibers for microwave absorption, Adv. Funct. Mater. 35 (2025) 2413650. https://doi.org/10.1002/adfm.202413650.

[39] Z. Xu, Y. Du, D. Liu, Y. Wang, W. Ma, Y. Wang, et al., Pea-like Fe/Fe_3C nanoparticles embedded in Nitrogen-doped carbon nanotubes with tunable dielectric/magnetic loss and efficient electromagnetic absorption, ACS Appl. Mater. Interfaces 11 (2019) 4268-4277. https://doi.org/10.1021/acsami.8b19201.

[40] Z. Ma, K. Yang, D. Li, H. Liu, S. Hui, Y. Jiang, et al., The electron migration polarization boosting electromagnetic wave absorption based on Ce atoms modulated yolk@shell Fe_xN@NGC, Adv. Mater. 36 (2024) 2314233. https://doi.org/10.1002/adma.202314233.

[41] L. Gai, H. Zhao, X. Li, P. Wang, S. Yu, Y. Chen, et al., Shell engineering afforded dielectric polarization prevails and impedance amelioration toward electromagnetic wave absorption enhancement in nested-network carbon architecture, Chem. Eng. J. 501 (2024) 157556. https://doi.org/10.1016/j.cej.2024.157556.

[42] J. Chen, C. Sun, Z. Han, Y. Zhang, F. Yang, L. Xing, et al., Rapidly synthesizing magneto-thermal adjustable high entropy alloy nanoparticles on carbon fiber surface for enhancing electromagnetic wave absorption, thermal conductivity and interface

compatibility of composites, Chem. Eng. J. 498 (2024) 155351. https://doi.org/10.1016/j.cej.2024.155351.

[43] J. Xiao, B. Zhan, X. Qi, J. Ding, Y. Qu, X. Gong, et al., Metal valence state modulation strategy to design core@shell hollow carbon microspheres@$MoSe_2$/MoO_x multicomponent composites for anti-corrosion and microwave absorption, Small 21 (2025) 2311312. https://doi.org/10.1002/smll.202311312.

[44] Y. Zhang, Y. Zhao, Q. Chen, Y. Hou, Q. Zhang, L. Cheng, et al., Flexible SiC-CNTs hybrid fiber mats for tunable and broadband microwave absorption, Ceram. Int. 47 (2021) 8123-8132. https://doi.org/10.1016/j.ceramint.2020.11.167.

[45] P. Wang, L. Gai, B. Hu, Y. Liu, F. Wang, P. Xu, et al., Topological MOFs deformation for the direct preparation of electromagnetic functionalized Ni/C aerogels with good hydrophobicity and thermal insulation, Carbon 212 (2023) 118132. https://doi.org/10.1016/j.carbon.2023.118132.

[46] Y. Zhao, J. Chua, Y. Zhang, W. Zhai, Development of multiscale Fe/SiC-C fibrous composites for broadband electromagnetic and acoustic waves absorption, Compos. Part B Eng. 250 (2023) 110454. https://doi.org/10.1016/j.compositesb.2022.110454.

[47] Y. Zhang, Y. Zhang, L. Yan, C. Liu, P. Ying, X. Li, et al., Simultaneous enhancement of low-frequency microwave absorption and corrosion resistance in FeSi alloys via magnetic-structural heterojunction engineering, Adv. Funct. Mater. (2025) 2508832. https://doi.org/10.1002/adfm.202508832.

[48] B. Li, J. Xu, H. Xu, F. Yan, X. Zhang, C. Zhu, et al., Grafting thin N-doped carbon nanotubes on hollow N-doped carbon nanoplates encapsulated with ultrasmall cobalt

particles for microwave absorption, Chem. Eng. J. 435 (2022) 134846. https://doi.org/10.1016/j.cej.2022.134846.

[49] X. Liu, Y. Duan, Y. Guo, Z. Li, J. Ma, J. Di, et al., In situ construction of complex spinel ferrimagnet in multi-elemental alloy for modulating natural resonance and highly efficient electromagnetic absorption, Chem. Eng. J. 462 (2023) 142200. https://doi.org/10.1016/j.cej.2023.142200.

[50] Y. Wang, X. Li, X. Han, P. Xu, L. Cui, H. Zhao, et al., Ternary Mo_2C/Co/C composites with enhanced electromagnetic waves absorption, Chem. Eng. J. 387 (2020) 124159. https://doi.org/10.1016/j.cej.2020.124159.

[51] Z. Ma, Y. Shen, X. Zhang, B. Li, Y. Chen, C. Zhu, Enhanced dielectric loss Induced by asymmetrically coordinated iron single-atoms with curved configurations on Turing-like surfaces for electromagnetic wave absorption, Adv. Funct. Mater. 35 (2025) 2413784. https://doi.org/10.1002/adfm.202413784.

[52] Z. Hou, X. Gao, J. Zhang, G. Wang, A perspective on impedance matching and resonance absorption mechanism for electromagnetic wave absorbing, Carbon 222 (2024) 118935. https://doi.org/10.1016/j.carbon.2024.118935.

[53] X. Jiang, B. Kang, X. Zhang, F. Yan, X. Zhang, F. Cao, et al., Short carbon nanorod-grafted N-doped carbon nanocages derived from LDH/MOFs for efficient electromagnetic wave absorption, Carbon 225 (2024) 119114. https://doi.org/10.1016/j.carbon.2024.119114.

[54] X. Shi, W. You, X. Li, L. Wang, Z. Shao, R. Che, In-situ regrowth constructed magnetic coupling 1D/2D Fe assembly as broadband and high-efficient microwave

absorber, Chem. Eng. J. 415 (2021) 128951. https://doi.org/10.1016/j.cej.2021.128951.

[55] H. Yuan, B. Li, C. Zhu, Y. Xie, Y. Jiang, Y. Chen, Dielectric behavior of single iron atoms dispersed on nitrogen-doped nanocarbon, Appl. Phys. Lett. 116 (2020) 153101. https://doi.org/10.1063/1.5143154.

[56] J. Du, T. Li, J. Li, J. Tang, R. Zhang, Y. Liu, et al., Design of flexible MXene/graphene-based fiber fabrics for broadband electromagnetic wave absorption, Adv. Fiber Mater. 7 (2025) 811-826. https://doi.org/10.1007/s42765-025-00523-y.

[57] C. Li, L. Liang, B. Zhang, Y. Yang, G. Ji, Magneto-dielectric synergy and multiscale hierarchical structure design enable flexible multipurpose microwave absorption and infrared stealth compatibility, Nano-Micro Lett. 17 (2025) 40. https://doi.org/10.1007/s40820-024-01549-4.

[58] X. Liu, J. Cai, J. Zhang, P. Zhao, G. Wang, S. Bi, et al., Surface-state-constrained topological insulator Bi_2Te_3 nanorods for electromagnetic wave trapping and conversion into electricity, J. Mater. Sci. Technol. 244 (2026) 149-155. https://doi.org/10.1016/j.jmst.2025.03.102.

[59] J. Li, T. Li, J. Du, J. Li, T. Liao, F. Meng, Optimization design of patterned rGO metasurface structures guided by electromagnetic simulation towards broadband electromagnetic wave absorption, Compos. Part B Eng. 298 (2025) 112378. https://doi.org/10.1016/j.compositesb.2025.112378.

[60] P. Liu, S. Gao, G. Zhang, Y. Huang, W. You, R. Che, Hollow engineering to Co@N-doped carbon nanocages via synergistic protecting-etching strategy for ultrahigh microwave absorption, Adv. Funct. Mater. 31 (2021) 2102812.

https://doi.org/10.1002/adfm.202102812.

[61] J. Li, S. Shuai, J. Wang, T. Li, J. Li, Z. Xu, et al., Dynamically adjustable absorbing performance under electrical stimulation and multifunctional integration of hybrid reduced graphene oxide/carbon foam, Chem. Eng. J. 506 (2025) 160338. https://doi.org/10.1016/j.cej.2025.160338.

[62] L. Lyu, F. Wang, X. Zhang, J. Qiao, C. Liu, J. Liu, CuNi alloy/carbon foam nanohybrids as high-performance electromagnetic wave absorbers, Carbon 172 (2021) 488-496. https://doi.org/10.1016/j.carbon.2020.10.021.

[63] L. Chang, Y. Wang, X. Zhang, L. Li, H. Zhai, M. Cao, Toward high performance microwave absorber by implanting $La_{0.8}CoO_3$ nanoparticles on rGO, J. Mater. Sci. Technol. 174 (2024) 176-187. https://doi.org/10.1016/j.jmst.2023.06.062.

[64] L. Rao, Z. Liu, L. Wang, W. You, C. Yang, R. Zhang, et al., Dimensional engineering of hierarchical nanopagodas for customizing cross-scale magnetic coupling networks to enhance electromagnetic wave absorption, Adv. Funct. Mater. 33 (2023) 2306984. https://doi.org/10.1002/adfm.202306984.

[65] P. Liu, Y. Li, H. Xu, L. Shi, J. Kong, X. Lv, et al., Hierarchical Fe-Co@TiO_2 with incoherent heterointerfaces and gradient magnetic domains for electromagnetic wave absorption, ACS Nano 18 (2024) 560-570. https://doi.org/10.1021/acsnano.3c08569.

[66] Z. Wu, Z. Yang, K. Pei, X. Qian, C. Jin, R. Che, Dandelion-like carbon nanotube assembly embedded with closely separated Co nanoparticles for high-performance microwave absorption materials, Nanoscale 12 (2020) 10149-10157. https://doi.org/10.1039/D0NR01447H.

[67] H. Zhou, Y. Lin, Y. Ma, L. Han, Z. Cai, Y. Cheng, et al., Hierarchical structure Fe@CNFs@Co/C elastic aerogels with intelligent electromagnetic wave absorption, InfoMat 7 (2025) e12630. https://doi.org/10.1002/inf2.12630.

[68] S. Guo, J. Zhang, C. Lin, J. Ge, S. Bi, Z. Hou, Multilayer core-shell structured $FeNi_3$@C with enhanced interfacial polarization for microwave absorbers, Nano Res. 18 (2025) 94907151. https://doi.org/10.26599/NR.2025.94907151.

[69] Y. Shi, X. Zhang, M. Liu, Z. Ma, C. Zhu, Y. Xie, et al., High-coordination engineering of asymmetrical cerium single-atoms for advanced electromagnetic wave absorption, Adv. Funct. Mater. (2025) 2504372. https://doi.org/10.1002/adfm.202504372.

[70] Y. Shi, B. Li, X. Jiang, X. Zhang, X. Zhang, Y. Chen, et al., The enhanced dielectric property of the graphene composite anchored with non-planar iron single-atoms, Appl. Phys. Lett. 121 (2022) 073102. https://doi.org/10.1063/5.0099781.

[71] J. Xu, M. Liu, X. Zhang, B. Li, X. Zhang, X. Zhang, et al., Atomically dispersed cobalt anchored on N-doped graphene aerogels for efficient electromagnetic wave absorption with an ultralow filler ratio, Appl. Phys. Rev. 9 (2022) 011402. https://doi.org/10.1063/5.0067791.

Declaration of interests

☒ The authors declare that they have no known competing financial interests or personal relationships that could have appeared to influence the work reported in this paper.

☐ The authors declare the following financial interests/personal relationships which may be considered as potential competing interests: